Experimental Observation of Dirac Nodal Links in Centrosymmetric Semimetal TiB$_2$

Zhonghao Liu,[1,*] Rui Lou,[2,*] Pengjie Guo,[2] Qi Wang,[2] Shanshan Sun,[2] Chenghe Li,[2] Setti Thirupathaiah,[3,4]
Alexander Fedorov,[3,5] Dawei Shen,[1] Kai Liu,[2,†] Hechang Lei,[2,‡] and Shancai Wang[2,§]

[1]State Key Laboratory of Functional Materials for Informatics and Center for Excellence in
Superconducting Electronics, SIMIT, Chinese Academy of Sciences, Shanghai 200050, China
[2]Department of Physics and Beijing Key Laboratory of Opto-electronic Functional Materials
& Micro-nano Devices, Renmin University of China, Beijing 100872, China
[3]Institute for Solid State Research, IFW Dresden, D-01171 Dresden, Germany
[4]Solid State and Structural Chemistry Unit, Indian Institute of Science,
Bangalore, Karnataka 560012, India
[5]Department of Physics, St. Petersburg State University, St. Petersburg 198504, Russia

The topological nodal-line semimetal state, serving as a fertile ground for various topological quantum phases, where a topological insulator, Dirac semimetal, or Weyl semimetal can be realized when the certain protecting symmetry is broken, has only been experimentally studied in very few materials. In contrast to discrete nodes, nodal lines with rich topological configurations can lead to more unusual transport phenomena. Utilizing angle-resolved photoemission spectroscopy and first-principles calculations, here, we provide compelling evidence of nodal-line fermions in centrosymmetric semimetal TiB$_2$ with a negligible spin-orbit coupling effect. With the band crossings just below the Fermi energy, two groups of Dirac nodal rings are clearly observed without any interference from other bands, one surrounding the Brillouin zone (BZ) corner in the horizontal mirror plane σ_h and the other surrounding the BZ center in the vertical mirror plane σ_v. The linear dispersions forming Dirac nodal rings are as wide as 2 eV. We further observe that the two groups of nodal rings link together along the Γ-K direction, composing a nodal-link configuration. The simple electronic structure with Dirac nodal links mainly constituting the Fermi surfaces suggests TiB$_2$ as a remarkable platform for studying and applying the novel physical properties related to nodal-line fermions.

Subject Areas: Condensed Matter Physics

I. INTRODUCTION

Topological materials with symmetry-protected nodes have recently attracted much attention in condensed matter physics. Perturbation that preserves a certain symmetry cannot remove the nodes by opening a full direct gap in these materials. When such nodes are close to the Fermi level (E_F), the low-energy quasiparticle excitations are drastically different from the usual Schrödinger-type fermions. These nodes can be classified by their dimensionality [1,2]. The zero-dimensional

ones include Dirac points, Weyl points, threefold degenerate points and other higher-fold degenerate nodal points. With the four- or twofold degenerate Dirac or Weyl points, respectively, Dirac and Weyl semimetals have been theoretically predicted and experimentally confirmed [3–12]. More recently, three-fold degenerate fermions, which conceptually lie between Dirac fermions and Weyl fermions, have been demonstrated to exist in the ZrTe family of compounds [13,14].

The nodal ring, nodal link, and nodal chain belong to the one-dimensional (1D) nodal-line systems whose nodes extend along 1D lines instead of discrete points in the three-dimensional (3D) Brillouin zone (BZ) [2,15–19]. Protected by the combination of spatial-inversion symmetry and time-reversal symmetry (the $P \cdot T$ symmetry) or certain crystalline symmetry [20,21], the nodal line may either take the form of an extended line running across the BZ, whose ends meet at the BZ boundary, or wind into a closed loop inside the BZ, or even form a chain consisting of several connected loops. A nontrivial Berry phase around the nodal lines would shift the Landau-level index by $1/2$ [17] and lead to drumhead surface states (SSs) [18,19].

Although band theory has predicted the existence of nodal-line fermions in some materials [19], only very

*These two authors contributed equally to this work.
†Corresponding author.
kliu@ruc.edu.cn
‡Corresponding author.
hlei@ruc.edu.cn
§Corresponding author.
scw@ruc.edu.cn

few candidates have been experimentally studied by angle-resolved photoemission spectroscopy (ARPES), i.e., CaAgAs, PbTaSe$_2$, and the ZrSiS family [20,22–26]. Very recently, two AlB$_2$-type diborides TiB$_2$ and ZrB$_2$ have been proposed to possess nodal-line configurations coexisting with a pair of the triply degenerate nodal points (TNPs) with negligible spin-orbit coupling (SOC) [27,28]. The formation of the TNPs was well uncovered by calculations, but these nodes cannot be observed by ARPES with the crossings located above E_F. On the other hand, the nodal lines could be clearly observed with the crossing located below E_F. In this work, we unambiguously identify two groups of Dirac nodal rings in TiB$_2$ by means of ARPES and first-principles calculations. The nodal rings embedded in the mirror plane σ_h (the Γ-K-M plane) around K points compose one group and those in the mirror plane σ_v (the Γ-A-H plane) around Γ point compose the other. Without interfering with other bands, the dispersions forming the nodal rings exhibit linearly in a wide energy range of approximately 2 eV. These two groups of nodal rings link together along the Γ-K direction forming a nodal-link configuration, which goes beyond the isolated nodal line configuration in other systems. The compelling evidences of the nodal-line

fermions existing just below E_F and the nodal links mainly constituting the Fermi surfaces (FSs) provide an ideal system for further investigations and potential applications on transport phenomena of nodal lines.

II. RESULTS AND DISCUSSION

TiB$_2$ has a simple AlB$_2$-type centrosymmetric structure with the space group $P6/mmm$ (No. 191) [29]. As shown in Fig. 1(a), titanium and boron atoms lie in planar close-packed hexagonal layers alternately. Figure 1(b) shows the x-ray diffraction (XRD) pattern of a TiB$_2$ crystal, indicating that the measured surface is the (00l) plane. The mirrorlike (001) surface is illustrated in the inset of Fig. 1(b). In Fig. 1(c), the zero-field resistivity ρ_{xx} of TiB$_2$ exhibits a metallic behavior in the measured temperature range from 3 to 300 K, and the magnetic field dependence of Hall resistivity ρ_{xy} at $T = 3$ K is displayed in the inset of Fig. 1(c). Based on the nonlinear feature of ρ_{xy} extending to high fields, electrons and holes are believed to coexist near E_F in TiB$_2$. Thus, we perform a quantitative analysis by fitting ρ_{xy} with the two-carrier model (superimposed on the original data) [30]. The extracted carrier densities of TiB$_2$ are $n_e = 2.74(4) \times 10^{21}$ cm^{-3} and
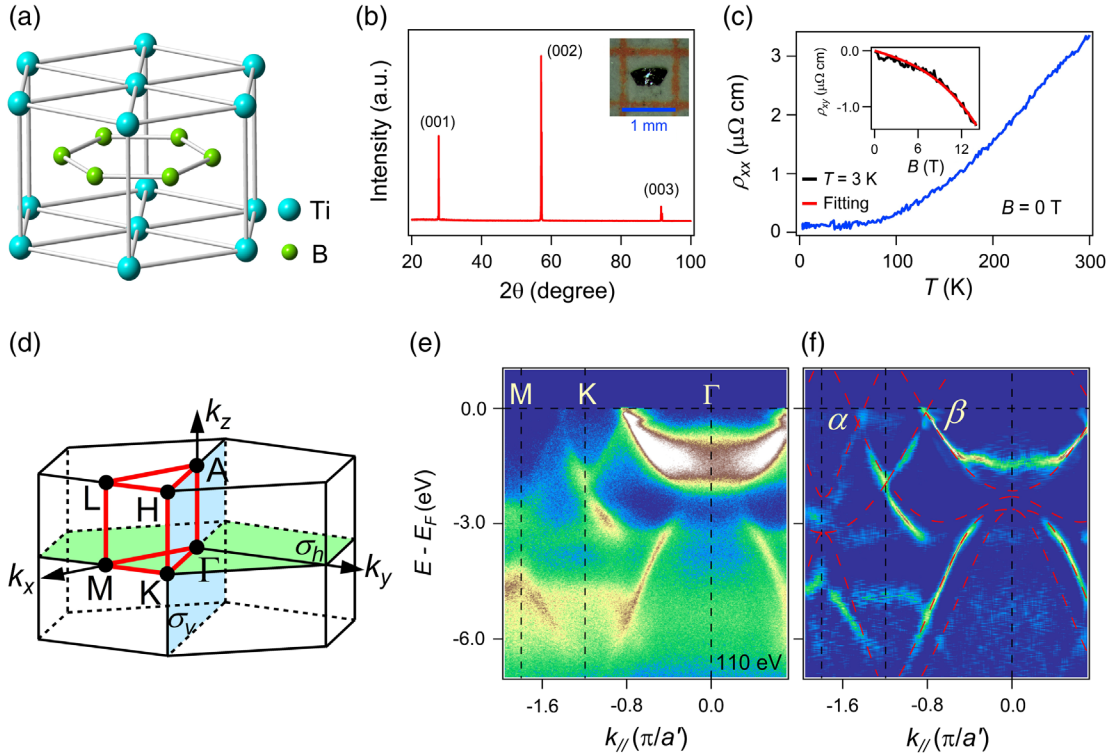

FIG. 1. Single-crystal and wide electronic structure of TiB$_2$. (a) Crystal structure of TiB$_2$ with space group $P6/mmm$ (No. 191). (b) XRD pattern of a TiB$_2$ single crystal. Inset: Picture of a TiB$_2$ crystal against the 1-mm scale. (c) Temperature dependence of the resistivity ρ_{xx} at $B = 0$ T. Inset: Hall resistivity ρ_{xy} (black curve) as a function of magnetic field ($B\|[001]$) at $T = 3$ K, with the superimposed fitting result (red curve) using the two-carrier model. (d) 3D bulk BZ with marked high-symmetry points and two mirror planes, σ_h (Γ-K-M plane) and σ_v (Γ-A-H plane). (e),(f) ARPES intensity plot and corresponding second derivative plot along the Γ-K-M direction. $a' = \sqrt{3}a/2$ ($a = 3.0335$ Å). The red curves in (f) represent the calculated bulk bands with SOC. The band-crossing features along the M-K and K-Γ directions are denoted as α and β, respectively.

$n_h = 2.63(4) \times 10^{21}$ cm^{-3}, respectively. They are much higher than those of Dirac semimetals like Na$_3$Bi (approximately 10^{17} cm^{-3} [31]) and Cd$_3$As$_2$ (approximately 10^{18} cm^{-3} [32]) with discrete nodes, but comparable to that of nodal-line semimetals ZrSiM ($M = S$, Se, and Te) (n_e, $n_h \sim 10^{20}$ cm^{-3} [33,34]). The concentrations in TiB$_2$ estimated from first-principles calculations (n_e, $n_h =$ 1.04, 1.10×10^{21} cm^{-3}) also show good consistency with experimental results.

The bulk BZ and high-symmetry points are indicated in Fig. 1(d). The Γ-K-M and Γ-A-H planes are two mirror planes (σ_h and σ_v) of the D_{6h} group, respectively. Figures 1(e) and 1(f) show the ARPES intensity plot in a wide energy region along the Γ-K-M direction and the corresponding second derivative plot, respectively. The calculated band dispersions have been superimposed on the second derivative plot, indicating the rather good agreement between the calculations and experimental data. Obviously, two linear band-crossing features denoted as α and β can be identified in Fig. 1(f).

To comprehensively and accurately investigate the electronic structure of TiB$_2$, we have scanned large portions of

k-space using various photon energies. The measured and calculated FSs are shown in Figs. 2(a)–2(d). Combining with the calculated band structure along high-symmetry lines, as displayed in Fig. 2(g), one can distinguish every FS in the whole 3D FS map of Fig. 2(c). Besides an electronlike and a holelike FS around the A point in the $k_z = \pi$ plane, the overall FSs are mainly composed of the nodal rings, with the nodal rings (r_1) embedded in the σ_h plane around K points linked with the ones (r_2) in the σ_v planes around the Γ point at J points along the Γ-K directions. Figure 2(d) shows the top view of the calculated 3D FSs, namely, the two-dimensional (2D) FSs projected on the (001) surface. With the FSs centered at the A point, the r_1 nodal ring surrounding the K point, the projection of the r_2 nodal ring around the Γ point, and the J nodal-link point all clearly resolved in Fig. 2(a), the experimental map taken with the photon energy of 80 eV well reproduces the feature of the 2D projected FSs. Because the ARPES spectra reflect the electronic states integrated over a certain k_z region of bulk BZ, and because the electronic states at $k_z = 0$ and π have main contributions [24,35], the r_1 nodal ring and the FSs centered at the A point could be prominently distinguished in a certain range of
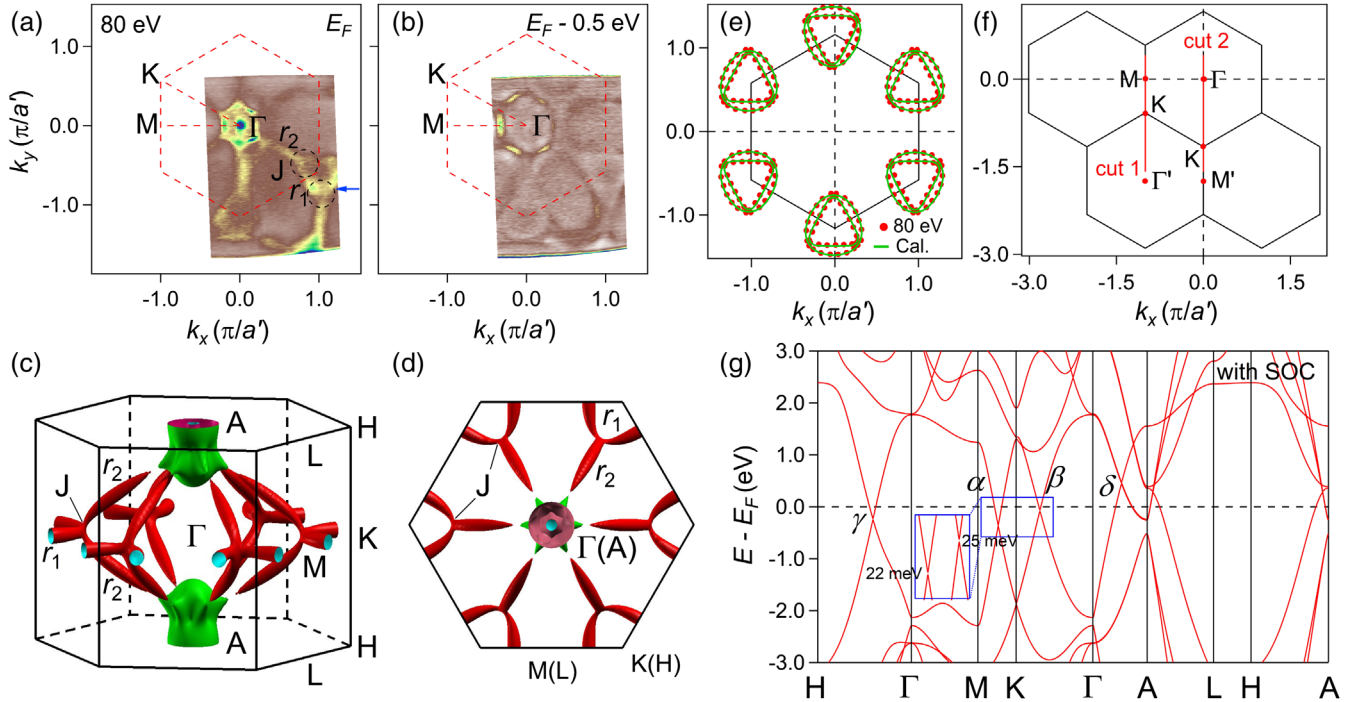

FIG. 2. FSs and calculated band structure of TiB$_2$. (a),(b) Intensity plots at E_F and 0.5 eV below E_F taken with 80-eV photons. The red dashed lines indicate high-symmetry directions and the first BZ projected on the (001) surface. Two groups of Dirac nodal rings r_1 and r_2 [projected on the (001) surface] are resolved. The link points (denoted as J points) of r_1 and r_2 are indicated by black dashed circles. (c),(d) Calculated bulk FSs in the 3D BZ and the top view of the FSs, respectively. The r_1 nodal ring surrounding the K point is embedded in the Γ-K-M plane. The r_2 nodal ring surrounding the Γ point is embedded in the Γ-A-H plane. (e) Comparison of the ARPES data and calculations for r_1. The green curves are calculated r_1 FSs. The red solid circles represent the experimental data, which are determined as follows: extracting the Fermi wave vectors from $1/3$ (marked by a blue arrow) of the r_1 nodal ring in (a); then, rotating it to a whole ring around the K point; and last, symmetrizing to obtain other rings in the BZ. (f) Schematic 2D BZs with marked cuts 1 and 2 indicating the momentum locations of the measured bands in Fig. 3. (g) Calculated bulk band structure along high-symmetry lines including SOC. Four near-E_F band-crossing features are denoted as α, β, γ, and δ, respectively. Inset: The enlarged view of α and β, small gaps of 22 and 25 meV open at the nodes, respectively, when SOC is taken into consideration.

photon energies. The banana-shaped r_1 nodal ring becomes a holelike pocket, when moving toward a high binding energy, as shown in Fig. 2(b).

In Fig. 2(g), one can find four band-crossing features near E_F along the M-K, K-Γ, H-Γ, and Γ-A directions, namely, α, β, γ, and δ, respectively. The nodes of the α and β band-crossing features are located below E_F; thus, all of the r_1 nodal rings are resolved in the FS map. The nodes of the γ and δ band-crossing features are below and above E_F, respectively, leading to the discontinuity of the r_2 nodal rings near the A point, as illustrated in Figs. 2(c) and 2(d). Also, under the protection of the C_{6v} symmetry along the Γ-A line, the node of the δ band-crossing feature is a TNP, which is formed by the crossing of a doubly degenerate band and a nondegenerate band. Because of time-reversal symmetry, a pair of the TNPs should locate at the two sides of the Γ point. Further, the SOC introduces small gaps of 22, 25, 22, and 33 meV to the nodes of α, β, γ, and δ, respectively [see the calculated bulk band structure without SOC in Fig. S1 of the Supplemental Material (SM) [36]]. The gap sizes are much less than those in CaAgAs (approximately 73 meV) [22] and ZrSiTe (approximately 60 meV) [26] and are comparable to those in ZrSiS and ZrSiSe (approximately 25–35 meV) [20,26], indicating the weak SOC effect on the bulk electronic structure of TiB_2. The r_2 nodal ring in the σ_v plane formed by γ and δ needs to be further demonstrated by the photon-energy-dependent studies, which will be discussed later. Here, we extract the Fermi wave vectors of r_1 according to the ARPES data and plot them in Fig. 2(e) with superimposed calculation contours. The size and shape of the calculated ones are very consistent with those determined by ARPES.

To quantitatively study the features of the r_1 nodal ring embedded in the σ_h plane, we record the ARPES spectra near E_F along the M-K and Γ-K directions, as indicated by cuts 1 and 2 in Fig. 2(f). The intensity plots and corresponding second derivative plots are presented in Figs. 3(a)–(d). The overall band structures agree well with the appended theoretical calculations. We also notice that some band dispersions near β along the Γ-K direction are not reproduced by bulk calculations. These bands most likely come from the contributions of bulk states in other k_z planes due to the k_z broadening effect [24,35].

To avoid the interference with other bands, we use the photon energy of 110 eV, in principle corresponding to the Γ-K-M plane, to record the intensity. As shown in Figs. 3(e)
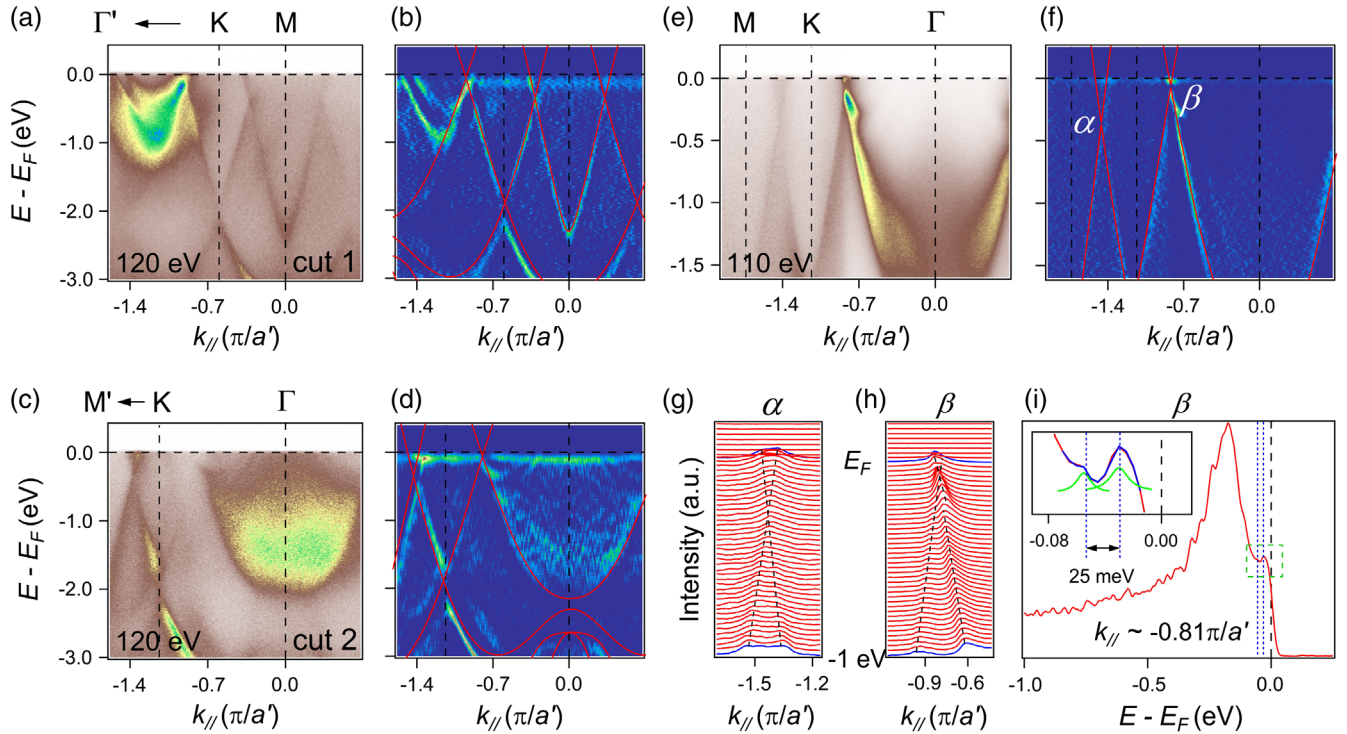

FIG. 3.   Electronic structure of the r_1 nodal ring. (a),(b) Intensity plot and corresponding second derivative plot along the M-K direction [cut 1 in Fig. 2(f)] recorded at $h\nu = 120$ eV ($k_z \sim 0.4\pi/c$). (c),(d) Same as (a),(b), but along the Γ-K direction [cut 2 in Fig. 2(f)]. (e),(f) Same as (a),(b), but recorded along the Γ-K-M direction with 110-eV photons ($k_z \sim 0$). The band-crossing features along the M-K and K-Γ directions, corresponding to the r_1 nodal ring surrounding the K point, are denoted as α and β in (f), respectively. The calculated bands with SOC are plotted on the second derivative plots in (b),(d), and (f). (g),(h) MDCs plots of α and β, respectively. The black dashed lines indicate the linear dispersions. (i) EDC taken at the center (approximately $-0.81\pi/a'$) of β. Inset: Zoomed in EDC near E_F indicated by the green dashed rectangle. By fitting the EDC with two Lorentzian profiles, shown as green curves, an opening gap of 25 meV can be determined. The blue curve is the superimposed fitting result.
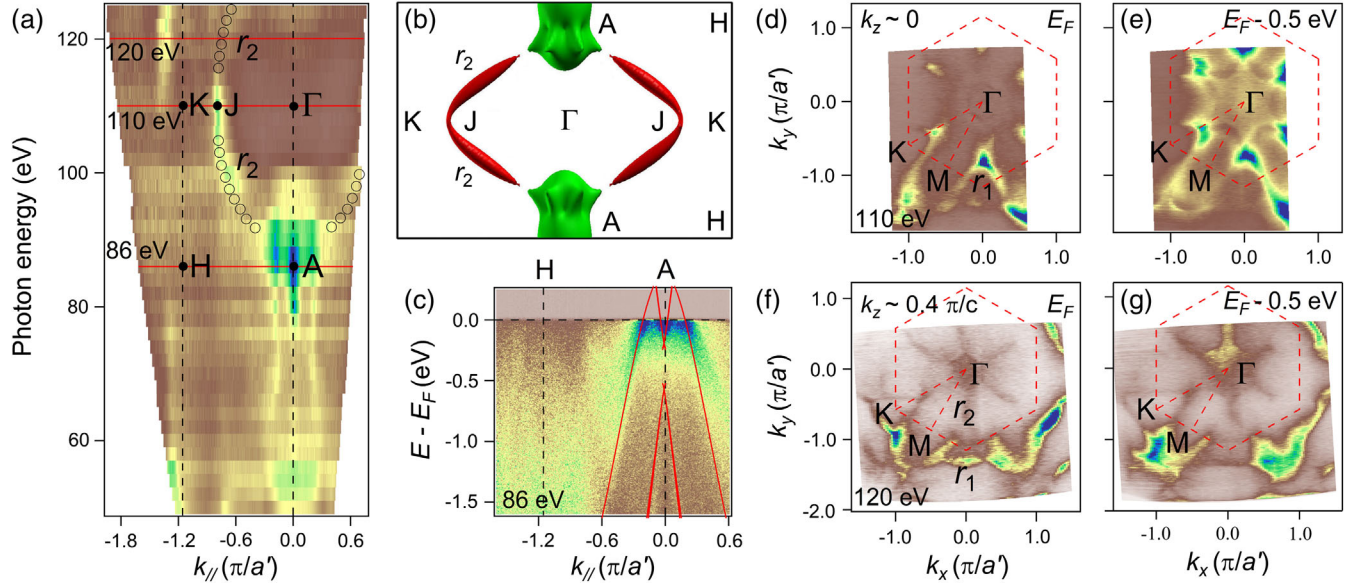
FIG. 4. Photon-energy-dependent dispersions of TiB$_2$. (a) Intensity plot in the $h\nu$-$k_{//}$ plane at E_F, with $k_{//}$ oriented along the Γ-K (A-H) direction. The high-symmetry points and nodal-link point are plotted. The r_2 nodal ring embedded in the Γ-A-H plane surrounding the Γ point is indicated by open circles. (b) Projections of calculated bulk FSs on the Γ-A-H plane. (c) ARPES spectra taken along the H-A line with 86-eV photons ($k_z \sim \pi$). The appended red curves are bulk band calculations with SOC. (d, e) Constant-energy ARPES images at E_F and 0.5 eV below E_F obtained by 110-eV photons ($k_z \sim 0$), respectively. (f),(g) Same as (d),(e), but taken with 120-eV photons ($k_z \sim 0.4\pi/c$).

and 3(f), the α and β band-crossing features are more outstandingly recognized. The corresponding momentum distribution curves (MDCs) in Figs. 3(g) and 3(h) unambiguously demonstrate the linear dispersions in a large energy range, and the nodes of α and β are below E_F. The sizes of α and β FSs along the Γ-K direction are 0.11 and 0.07π/a', respectively. The result is in agreement with the data extracted from de Haas–van Alphen effect measurements [37]. To quantitatively determine the energy gaps at the nodes, we extract the energy distribution curve (EDC) at the center (about $-0.81\pi/a'$) of β, as illustrated in Fig. 3(i). By zooming in the near-E_F area, one can clearly see two peaks in the inset of Fig. 3(i). We use two Lorentzian curves to fit this single EDC and superimpose the fitting result as a blue curve. The gap of approximately 25 meV at the node of β can be obtained, showing good consistency with theoretical calculation. Although the faint intensity due to the matrix element effect obstructs the determination of the band gap at α, we can reasonably expect a small gap opening based on the high consistency between experiments and calculations.

As mentioned above, the r_2 nodal ring embedded in the σ_v plane needs to be further demonstrated in the $k_z - k_{//}$ plane. We perform k_z-dependent measurements by varying the photon energy from 50 to 124 eV, covering more than one BZ along the k_z direction. Figure 4(a) shows the intensity plot at E_F as a function of photon energy and $k_{//}$, which is oriented along the Γ-K (A-H) direction. One can see that the photoemission intensity is enhanced around the A point (86 eV) and suppressed around the Γ point (110 eV) along the A-Γ direction, showing a periodic modulation

along with photon energies. By comparing with the projections of calculated FSs on the Γ-A-H plane in Fig. 4(b), the r_2 nodal rings passing through the J nodal-link point are traced out by open circles in Fig. 4(a). With the observation of both the (001) projection and the 3D character of the r_2 nodal ring in Figs. 2(a) and 4(a), respectively, the existence of nodal rings embedded in the σ_v planes can be clearly proved. Thus, the nodal-link structure formed by the r_1 and r_2 nodal rings is confirmed.

Figure 4(c) shows the ARPES intensity plot along the A-H line taken by the photon energy of 86 eV. As compared with the band structure along the Γ-K direction in Fig. 3(e), an electronlike band and a holelike band cross E_F around the A point, while no band exists at the Γ point. Moreover, the β band-crossing feature along the Γ-K direction disappears along the A-H direction. These contrasts reveal the 3D nature of the band structure around the A point and the embedding of the r_1 nodal ring in the σ_h plane. Figures 4(d)–4(g) show the constant-energy maps in the k_x-k_y plane, which are taken by the photon energies of 110 eV ($k_z \sim 0$) and 120 eV ($k_z \sim 0.4\pi/c$), respectively. As illustrated in Fig. 4(f), the nodal-link configurations of r_1 and r_2 are also recognized like that in Fig. 2(a).

Besides the bulk evidence of the nodal line, the drumhead SSs appearing inside the projections of the nodal lines serve as the surface signature. As discussed above, small gaps will open at the nodes of α, β, γ, and δ, when including the SOC effect. Given the presence of the inversion center in TiB$_2$, we calculate the product of the parities of the occupied states, which are all doubly degenerate due to the $P \cdot T$ symmetry, at

the eight time-reversal invariant momenta with SOC [38]. The results are listed in Table S1 of the SM [36]. With a Z_2 index as (0; 001), the SSs of TiB$_2$ predicted in Refs. [27,28] are not topologically protected, and a small perturbation on the surface could hinder the observation of SSs in our experiments.

III. CONCLUSION

By systematically mapping out the 3D electronic structure both in experiment and theory, we unambiguously demonstrate the existence of nodal-line fermions in TiB$_2$, hosting Dirac nodal links formed by two groups of nodal rings with a negligible SOC effect, under the protection of $P \cdot T$ symmetry and certain mirror reflection symmetries. The discovered features, i.e., the nodal-line fermions existing just below E_F and the nodal links mainly constituting the FSs, must have a significant contribution to the low-energy excitations. The simple electronic structure composed of a large energy range of linearly dispersive bands offers a good platform for further studies into Dirac physics.

ACKNOWLEDGMENTS

APPENDIX: MATERIALS AND METHODS

1. Sample synthesis

Single crystals of TiB$_2$ were grown by the Co flux method. The starting elements of Ti (99.995%), B (99.99%), and Co (99.99%) were put into an alumina crucible, with a molar ratio of Ti:B:Co = 1:2:4. The mixture was heated up to 1873 K in a high-purity argon atmosphere and then slowly cooled down to 1623 K at a rate of 4 K/h. The TiB$_2$ single crystals were separated from the Co flux using a hot hydrochloric acid solution.

2. ARPES measurements

ARPES measurements were performed at the UE112_ PGM-2 ARPES end station of BESSY using photon energies from 50 to 124 eV. The energy and angular resolutions were set to 15 meV and 0.2°, respectively. Samples were cleaved *in situ*, yielding flat mirrorlike (001)

surfaces. During the measurements, the temperature was kept at 40 K and the pressure was maintained greater than 5×10^{-11} Torr.

3. Band structure calculations

First-principles electronic structure calculations on TiB$_2$ were carried out with the projector augmented wave method [39,40] as implemented in the Vienna *ab initio* Simulation Package [41]. The generalized gradient approximation of the Perdew-Burke-Ernzerhof formula [42] was adopted for the exchange-correlation functional. The kinetic energy cutoff of the plane-wave basis was set to be 420 eV. A $20 \times 20 \times 20$ k-point mesh was utilized for the BZ sampling. The FSs were investigated by adopting the maximally localized Wannier function method [43]. The SOC effect was taken into account in all of the above calculations.

[1] C. K. Chiu, J. C. Y. Teo, A. P. Schnyder, and S. Ryu, *Classification of Topological Quantum Matter with Symmetries*, Rev. Mod. Phys. **88**, 035005 (2016).

[2] A. A. Burkov, M. D. Hook, and L. Balents, *Topological Nodal Semimetals*, Phys. Rev. B **84**, 235126 (2011).

[3] Z. K. Liu, B. Zhou, Y. Zhang, Z. J. Wang, H. M. Weng, D. Prabhakaran, S. K. Mo, Z. X. Shen, Z. Fang, X. Dai, Z. Hussain, and Y. L. Chen, *Discovery of a Three-Dimensional Topological Dirac Semimetal,* Na$_3$Bi, Science **343**, 864 (2014).

[4] S. Borisenko, Q. Gibson, D. Evtushinsky, V. Zabolotnyy, B. Büchner, and R. J. Cava, *Experimental Realization of a Three-Dimensional Dirac Semimetal*, Phys. Rev. Lett. **113**, 027603 (2014).

[5] H. M. Weng, C. Fang, Z. Fang, B. A. Bernevig, and X. Dai, *Weyl Semimetal Phase in Noncentrosymmetric Transition-Metal Monophosphides*, Phys. Rev. X **5**, 011029 (2015).

[6] S. M. Huang, S. Y. Xu, I. Belopolski, C. Lee, G. Chang, B. Wang, N. Alidoust, G. Bian, M. Neupane, C. Zhang, S. Jia, A. Bansil, H. Lin, and M. Z. Hasan, *A Weyl Fermion Semimetal with Surface Fermi Arcs in the Transition Metal Monopnictide TaAs Class*, Nat. Commun. **6**, 7373 (2015).

[7] X. Huang, L. Zhao, Y. Long, P. Wang, D. Chen, Z. Yang, H. Liang, M. Xue, H. Weng, Z. Fang, X. Dai, and G. Chen, *Observation of the Chiral-Anomaly-Induced Negative Magnetoresistance in 3D Weyl Semimetal TaAs*, Phys. Rev. X **5**, 031023 (2015).

[8] S. Y. Xu *et al.*, *Discovery of a Weyl Fermion Semimetal and Topological Fermi Arcs*, Science **349**, 613 (2015).

[9] B. Q. Lv, H. M. Weng, B. B. Fu, X. P. Wang, H. Miao, J. Ma, P. Richard, X. C. Huang, L. X. Zhao, G. F. Chen, Z. Fang, X. Dai, T. Qian, and H. Ding, *Experimental Discovery of Weyl Semimetal TaAs*, Phys. Rev. X **5**, 031013 (2015).

[10] L. X. Yang, Z. K. Liu, Y. Sun, H. Peng, H. F. Yang, T. Zhang, B. Zhou, Y. Zhang, Y. F. Guo, M. Rahn, D. Prabhakaran, Z. Hussain, S.-K. Mo, C. Felser, B. Yan, and Y. L. Chen, *Weyl Semimetal Phase in the Non-Centrosymmetric Compound TaAs*, Nat. Phys. **11**, 728 (2015).

[11] S. Y. Xu *et al.*, *Discovery of a Weyl Fermion State with Fermi Arcs in Niobium Arsenide*, Nat. Phys. **11,** 748 (2015).

[12] N. Xu, H. M. Weng, B. Q. Lv, C. E. Matt, J. Park, F. Bisti, V. N. Strocov, D. Gawryluk, E. Pomjakushina, K. Conder, N. C. Plumb, M. Radovic, G. Autès, O. V. Yazyev, Z. Fang, X. Dai, T. Qian, J. Mesot, H. Ding, and M. Shi, *Observation of Weyl Nodes and Fermi Arcs in Tantalum Phosphide*, Nat. Commun. **7,** 11006 (2016).

[13] Z. Zhu, G. W. Winkler, Q. S. Wu, J. Li, and A. A. Soluyanov, *Triple Point Topological Metals*, Phys. Rev. X **6,** 031003 (2016).

[14] B. Q. Lv, Z. L. Feng, Q. N. Xu, X. Cao, J. Z. Ma, L. Y. Kong, P. Richard, Y. B. Huang, V. N. Strocov, C. Fang, H. M. Wang, Y. G. Shi, T. Qian, and H. Ding, *Observation of Three-Component Fermions in the Topological Semimetal Molybdenum Phosphide*, Nature (London) **546,** 627 (2017).

[15] C. Fang, Y. Chen, H. Y. Kee, and L. Fu, *Topological Nodal Line Semimetals with and without Spin-Orbital Coupling*, Phys. Rev. B **92,** 081201 (2015).

[16] T. Bzdušek, Q. Wu, A. Rüegg, M. Sigrist, and A. A. Soluyanov, *Nodal-Chain Metals*, Nature (London) **538,** 75 (2016).

[17] Z. Yan, R. Bi, H. Shen, L. Lu, S. C. Zhang, and Z. Wang, *Nodal-Link Semimetals*, Phys. Rev. B **96,** 041103(R) (2017).

[18] C. Fang, H. M. Weng, X. Dai, and Z. Fang, *Topological Nodal Line Semimetals*, Chin. Phys. B **25,** 117106 (2016).

[19] R. Yu, Z. Fang, X. Dai, and H. Weng, *Topological Nodal Line Semimetals Predicted from First-Principles Calculations*, Front. Phys. **12,** 127202 (2017).

[20] L. M. Schoop, M. N. Ali, C. Straßer, A. Topp, A. Varykhalov, D. Marchenko, V. Duppel, S. S. P. Parkin, B. V. Lotsch, and C. R. Ast, *Dirac Cone Protected by Non-Symmorphic Symmetry and Three-Dimensional Dirac Line Node in ZrSiS*, Nat. Commun. **7,** 11696 (2016).

[21] Q. Xu, R. Yu, Z. Fang, X. Dai, and H. Weng, *Topological Nodal Line Semimetals in the* CaP_3 *Family of Materials*, Phys. Rev. B **95,** 045136 (2017).

[22] X.-B. Wang, X.-M. Ma, E. Emmanouilidou, B. Shen, C.-H. Hsu, C.-S. Zhou, Y. Zuo, R.-R. Song, S.-Y. Xu, G. Wang, L. Huang, N. Ni, and C. Liu, *Topological Surface Electronic States in Candidate Nodal-Line Semimetal CaAgAs*, Phys. Rev. B **96,** 161112(R) (2017).

[23] G. Bian *et al.*, *Topological Nodal-Line Fermions in Spin-Orbit Metal* $PbTaSe_2$, Nat. Commun. **7,** 10556 (2016).

[24] D. Takane, Z. Wang, S. Souma, K. Nakayama, C. X. Trang, T. Sato, T. Takahashi, and Y. Ando, *Dirac-Node Arc in the Topological Line-Node Semimetal HfSiS*, Phys. Rev. B **94,** 121108(R) (2016).

[25] R. Lou, J.-Z. Ma, Q.-N. Xu, B.-B. Fu, L.-Y. Kong, Y.-G. Shi, P. Richard, H.-M. Weng, Z. Fang, S.-S. Sun, Q. Wang, H.-C. Lei, T. Qian, H. Ding, and S.-C. Wang, *Emergence of Topological Bands on the Surface of ZrSnTe Crystal*, Phys. Rev. B **93,** 241104(R) (2016).

[26] M. M. Hosen, K. Dimitri, I. Belopolski, P. Maldonado, R. Sankar, N. Dhakal, G. Dhakal, T. Cole, P. M. Oppeneer, D. Kaczorowski, F. Chou, M. Z. Hasan, T. Durakiewicz, and M. Neupane, *Tunability of the Topological Nodal-Line Semimetal Phase in ZrSiX-Type Materials (X = S, Se, Te)*, Phys. Rev. B **95,** 161101(R) (2017).

[27] X. Zhang, Z. M. Yu, X. L. Sheng, H. Y. Yang, and S. A. Yang, *Coexistence of Four-Band Nodal Rings and Triply Degenerate Nodal Points in Centrosymmetric Metal Diborides*, Phys. Rev. B **95,** 235116 (2017).

[28] X. Feng, C. Yue, Z. Song, Q. Wu, and B. Wen, *Topological Dirac Nodal-Net Fermions in* AlB_2-*Type* TiB_2 *and* ZrB_2, Phys. Rev. Mater. **2,** 014202 (2018).

[29] B. Post, F. W. Glaser, and D. Moskowitz, *Transition Metal Diborides*, Acta Metall. **2,** 20 (1954).

[30] B. Xia, P. Ren, A. Sulaev, P. Liu, S.-Q. Shen, and L. Wang, *Indications of Surface-Dominated Transport in Single Crystalline Nanoflake Devices of Topological Insulator* $Bi_{1.5}Sb_{0.5}Te_{1.8}Se_{1.2}$, Phys. Rev. B **87,** 085442 (2013).

[31] J. Xiong, S. K. Kushwaha, T. Liang, J. W. Krizan, M. Hirschberger, W. Wang, R. J. Cava, and N. P. Ong, *Evidence for the Chiral Anomaly in the Dirac Semimetal* Na_3Bi, Science **350,** 413 (2015).

[32] T. Liang, Q. Gibson, M. N. Ali, M. Liu, R. J. Cava, and N. P. Ong, *Ultrahigh Mobility and Giant Magneto-resistance in the Dirac Semimetal* Cd_3As_2, Nat. Mater. **14,** 280 (2015).

[33] J. Hu, Z. Tang, J. Liu, X. Liu, Y. Zhu, D. Graf, K. Myhro, S. Tran, C. N. Lau, J. Wei, and Z. Mao, *Evidence of Topological Nodal-Line Fermions in ZrSiSe and ZrSiTe*, Phys. Rev. Lett. **117,** 016602 (2016).

[34] J. Hu, Z. Tang, J. Liu, Y. Zhu, J. Wei, and Z. Mao, *Nearly Massless Dirac Fermions and Strong Zeeman Splitting in the Nodal-Line Semimetal ZrSiS Probed by De Haas-Van Alphen Quantum Oscillations*, Phys. Rev. B **96,** 045127 (2017).

[35] H. Kumigashira, H.-D. Kim, T. Ito, A. Ashihara, T. Takahashi, T. Suzuki, M. Nishimura, O. Sakai, Y. Kaneta, and H. Harima, *High-Resolution Angle-Resolved Photoemission Study of LaSb*, Phys. Rev. B **58,** 7675 (1998).

[36] See Supplemental Material at http://link.aps.org/supplemental/10.1103/PhysRevX.8.031044 for bulk band calculations without SOC, EDX, powder XRD, field dependence of the resistivity and Hall resistivity at $T = 3$ K, slab calculation with 20 unit cells, and the parity products for the occupied states at the time-reversal invariant momenta.

[37] T. Tanaka and Y. Ishizawa, *The De Haas-Van Alphen Effect in* TiB_2, J. Phys. C **13,** 6671 (1980).

[38] L. Fu, C. L. Kane, and E. J. Mele, *Topological Insulators in Three Dimensions*, Phys. Rev. Lett. **98,** 106803 (2007).

[39] P. E. Blöchl, *Projector Augmented-Wave Method*, Phys. Rev. B **50,** 17953 (1994).

[40] G. Kresse and D. Joubert, *From Ultrasoft Pseudopotentials to the Projector Augmented-Wave Method*, Phys. Rev. B **59,** 1758 (1999).

[41] G. Kresse and J. Hafner, *Ab Initio Molecular Dynamics for Open-Shell Transition Metals*, Phys. Rev. B **48,** 13115 (1993).

[42] J. P. Perdew, K. Burke, and M. Ernzerhof, *Generalized Gradient Approximation Made Simple*, Phys. Rev. Lett. **77,** 3865 (1996).

[43] I. Souza, N. Marzari, and D. Vanderbilt, *Maximally Localized Wannier Functions for Entangled Energy Bands*, Phys. Rev. B **65,** 035109 (2001).